Materials Today Bio 32 (2025) 101748

Contents lists available at ScienceDirect

Materials Today Bio

journal homepage: www.journals.elsevier.com/materials-today-bio

A novel therapeutic approach to hemangiomas: Combining photothermal therapy and ferroptosis in a microneedle delivery system

Yiming Geng [a,1], Cancan Meng [a,1], Hanzhi Zhang [a,b,1], Chuan Ma [c,*], Xiao Fu [a,b,**], Haiwei Wu [a,***]

[a] Department of Oral and Maxillofacial Surgery, Shandong Provincial Hospital Affiliated to Shandong First Medical University, Jinan, Shandong, 250021, China
[b] School of Stomatology, Shandong First Medical University & Shandong Academy of Medical Sciences, Jinan, Shandong, 250117, China
[c] Department of Oral and Maxillofacial Surgery, School and Hospital of Stomatology, Cheeloo College of Medicine, Shandong University & Shandong Key Laboratory of Oral Tissue Regeneration & Shandong Engineering Research Center of Dental Materials and Oral Tissue Regeneration & Shandong Provincial Clinical Research Center for Oral Diseases, China

ARTICLE INFO

Keywords:
Hemangioma
Anti-angiogenesis
Microneedle patch
Ferroptosis therapy
Photothermal effect

ABSTRACT

Infantile Hemangioma (IH) is the most common benign vascular tumor occurred in infants and young children. The larger hemangiomas or lesions located in specific areas can cause severe complications, such as disfigurement, obstruction, or ulceration, increasing the risk of functional impairment. Propranolol, serving as the first-line drug for IH treatment, still poses various challenges. Certain patients exhibit low sensitivity to propranolol therapy or face recurrence, which become the leading reason for the failure of IH treatment. Additionally, the requirement for frequent daily medication can also complicate adherence for patients. Hence, developing novel IH therapy methods or drug administration routes is significantly important to enhance therapeutic effect and reduce side effects. Accordingly, in this study, we introduced an innovative photothermal, dissolving microneedles (MNs) patch designed specifically for IH therapy. Firstly, a pH responsive self-assembly nanoplatform with photothermal effect is designed by encapsulating propranolol (PRN) into zeolitic imidazolate framework-8 (ZIF-8) NPs and modifying with TA/Fe nanocomplexes. The fabricated PRN@ZIF-8@TA/Fe (PZ@TA/Fe) NPs exhibited good biocompatibility, pH-responsive degradation, photothermal conversion efficiency inside hemangioma endothelial cells (HemECs). Importantly, TA/Fe surface modification led to intracellular iron overload, which subsequently induced the Fenton reaction and triggered ferroptosis process. The combination of photothermal therapy and ferroptosis therapy exhibited a superior synergistic effect in damaging HemECs and vascular structures. The PZ@TA/Fe NPs loaded in MNs patch further ensured targeted delivery to lesion areas and achieved precise and maximal release of the PZ@TA/Fe NPs, while reducing systemic side effects to normal vasculature or tissue. The PZ@TA/Fe@MNs showed remarkable anti-angiogenic effect against IH in mice model. This study first investigates the potential of ferroptosis therapy in IH treatment, and highlights the substantial therapeutic effect of combining photothermal therapy and ferroptosis effects against IH proliferation. This approach can also become a more effective and safer treatment method for other diseases characterized by abnormal angiogenesis.

* Corresponding author. Department of Oral and Maxillofacial Surgery, School and Hospital of Stomatology, Cheeloo College of Medicine, Shandong University & Shandong Key Laboratory of Oral Tissue Regeneration & Shandong Engineering Research Center of Dental Materials and Oral Tissue Regeneration & Shandong Provincial Clinical Research Center for Oral Diseases, China, No.44-1 Wenhua Road West, 250012, Jinan, Shandong, China.
** Corresponding author. Department of Oral and Maxillofacial Surgery, Shandong Provincial Hospital Affiliated to Shandong First Medical University, 324 Jingwu Road, Jinan, 250021, China.
*** Corresponding author. Department of Oral and Maxillofacial Surgery, Shandong Provincial Hospital Affiliated to Shandong First Medical University, 324 Jingwu Road, Jinan, 250021, China.
E-mail addresses: machuan@sdu.edu.cn (C. Ma), fuxiao@sdfmu.edu.cn (X. Fu), hwwu0804@163.com (H. Wu).
[1] **Co-first authorship**, These authors contributed equally to this work.

https://doi.org/10.1016/j.mtbio.2025.101748
Received 16 January 2025; Received in revised form 21 March 2025; Accepted 8 April 2025
Available online 9 April 2025

1. Introduction

Hemangioma is the most common benign vascular tumor, with historical incidence rates between 5 and 10 % [1–3]. Hemangioma possesses a unique growth pattern characterized by a rapid proliferative phase, followed by spontaneous involution [4,5]. During the proliferative phase, hemangiomas can grow rapidly within the first three to six months after birth and then gradually transform into fibrofatty tissue over the years [6,7]. However, some hemangiomas can result in permanent lesions. Approximately 10–15% of larger hemangiomas, or those found in specific areas, such as the neck, head, anal, and perineal regions, can lead to various complications like disfigurement, obstruction, or ulceration, increasing the risk of functional impairment [2]. Hence, in addition to hemangiomas located in non-cosmetically sensitive areas that are stable and cannot cause functional impairment, active treatments should be pursued for hemangioma lesions that exhibit progressive characteristics or complications [8].

Currently, the clinical treatment methods for hemangiomas mainly include surgery, laser therapy, and drug therapy [9–11]. Although surgery and laser therapy can obtain effective therapeutic effects, these methods may exert a relatively high cost and surgery may lead to scar remnants or tissue defects. As a result, non-invasive, convenient and cost-effective drug therapy has gradually become preferred treatment option. In 2008, Léauté-Labrèze et al. demonstrated that Propranolol (PRN), a nonselective β-adrenergic receptor blocker, could decelerate or manage the growth of hemangioma effectively [12]. After that, PRN has become the first-line therapy for hemangioma of infancy. Recently, PRN has been formulated in various dosage forms in clinical application, such as oral tablets, ointments, gels, eye drops [13–15]. However, existing drug formulations have various disadvantages. Oral administration often presents several challenges, particularly in achieving effective drug concentrations at targeted sites. This method can result in limited drug accumulation, leading to low bioavailability and a short half-life of the active compound. Additionally, drugs in circulation may reach unintended sites, causing off-target effects and potential toxicity to healthy tissues, which compromises treatment efficacy and patient safety. In the case of PRN, high-dose oral administration is associated with a range of adverse reactions. Such side effects include significant hypotension, bradycardia, hyperkalemia, bronchospasm, and hypoglycemia. These reactions pose serious risks to patients, and their potential occurrence necessitates careful dose management and monitoring [16–18]. In contrast, transdermal drug delivery systems have emerged as a promising therapeutic modality for superficial hemangiomas, offering localized drug deposition and reduced systemic exposure compared to oral or injectable therapies. However, due to the tough stratum corneum, current transdermal drug delivery methods face challenges in inefficiently delivering agents to the deeper dermis and subcutaneous tissue layers [19]. Research indicated that cream formulations typically allowed only 10–20 % of the total drug content to permeate adequately [19,20]. This inherent limitation stems from the corneocyte lipid matrix, which restricts hydrophilic molecule diffusion and hydrophobic compound partitioning. Mechanistic studies have revealed that standard topical formulations, such as hydrogels and ointments, often fail to achieve therapeutic concentrations in the deeper dermis and subcutaneous tissues where hemangioma endothelial cells reside. These disadvantages may result in incomplete fading of lesions, with some patients not responding to such superficial treatments effectively. Consequently, there is an urgent need to explore more effective topical strategies that are minimally invasive, efficient, user-friendly, and safe for the treatment of hemangioma.

Over the past few years, microneedles (MNs) have garnered significant interest as a promising approach in the treatment of various diseases. MNs, composed of hundreds of micro-scaled needles arranged in an array, can break the stratum corneum layer and provide a clear pathway to deliver therapeutic drugs to lesion area directly [21]. Compared with traditional oral and transdermal administration, MNs can avoid gastrointestinal absorption and improve drug permeation efficiency through the skin [22]. Various materials for MNs have been explored and developed for drug delivery, primarily including solid, coated, hollow, and dissolving MNs [23,24]. Due to the bio-acceptability and dissolution of polymer inside the skin, dissolving MNs are considered one of the best options for long-term hemangiomas therapy. In addition, the customizability of microneedle size, including patch size and tip heigh, can obtain the specific needs of individual patients in clinical applications.

Combining multiple treatment modalities may enable the efficient management of hemangiomas and accelerate lesion regression. Photothermal therapy (PTT) utilizes photothermal conversion agents (PTAs) to produce enough heat under near-infrared (NIR) laser irradiation to induce cell death (temperatures higher than 45 °C) or enhance the sensitivity of cells to other therapies (temperatures between 40 and 45 °C), which compensates for the limitations of hemangiomas treatment, thereby enhancing the overall therapeutic efficacy [25,26]. In contrast with traditional radiotherapy or chemotherapy, PTT possesses some attractive advantages, such as minimal invasiveness, high specificity and reduced side effects [27]. Moreover, PTT has a great selectivity due to the controllability of various laser irradiation parameters (e.g., laser wavelength, location, light intensity and irradiation time) [28,29]. Hence, PTAs are critical components for PTT to induce a localized temperature rise. Metal-phenolic networks (MPNs) are considered promising materials owing to versatile properties and potential applications in biomedical applications [30,31]. MPNs are formed through the coordination of metal ions with phenolic ligands [32]. Tannic acid (TA) contains multiple phenol hydroxy structures that can serve as multi-ligands, enabling to chelate various metal ions and thus create stable metal–organic complexes [33]. Significantly, the TA/Fe nanocomplexes have excellent photothermal effect and can form a coating with an adjustable thickness at the interface of nanoparticles [34,35]. Moreover, TA/Fe nanocomplexes can degrade and release Fe to sustain Fenton reaction and induce ferroptosis process. Ferroptosis, an iron-dependent form of programmed cell death, has attracted much attention as a novel anti-tumor strategy [36–38]. Importantly, emerging evidence highlights ferroptosis as a tumor-suppressive mechanism during hemangioma involution. Involutive IH lesions exhibit marked elevation of 4-hydroxynonenal (4-HNE), a marker of lipid peroxidation and ferroptosis. In addition, IH lesions show elevated GPX4 expression in macrophages, a key enzyme that suppresses ferroptosis, indicating that macrophage ferroptosis resistance supports lesion progression. Reducing the resistance by inhibiting GPX4 in macrophages can effectively promote the regression of IH. Thus, ferroptosis may serve as a novel mechanism in HemSCs reprogramming the microenvironment [39]. However, ferroptosis therapy has been rarely investigated and attempted in the treatment of hemangiomas recently. Endogenous hydrogen peroxide (H_2O_2) can be transformed into a cytotoxic hydroxyl radical (•OH) through Fenton or Fenton-like reactions, which leads to dysfunction of cellular antioxidant systems and stimulates the formation of intracellular lipid peroxides, ultimately inducing ferroptosis [40–42]. However, Fe(II), the key element to induce ferroptosis, is susceptible to oxidation to Fe(III) by oxygen and then inhibit the ability to catalyze the Fenton reaction [43]. Surprisedly, TA possesses reducing properties and can reduce Fe(III) to Fe(II) both in vitro and in vivo, which enhance the efficiency of the Fenton reaction. Hence, TA/Fe nanocomplexes can be considered as an ideal surface modification for nano materials. Moreover, the ferroptosis therapy may become a potential therapy method for hemangiomas.

Above all, aiming at exerting an anti-angiogenic effect to treat hemangioma, we designed and synthesized an innovative photothermal, dissolving microneedle patch (Scheme 1). In these MNs, propranolol (PRN) was encapsulated into zeolitic imidazolate framework (ZIF-8). ZIF-8 has been widely used as the drug carriers due to remarkable advantages, such as good biocompatibility, high porosity, and degradation at low pH [44]. The synthesized PRN@ZIF-8 (PZ) were modified with

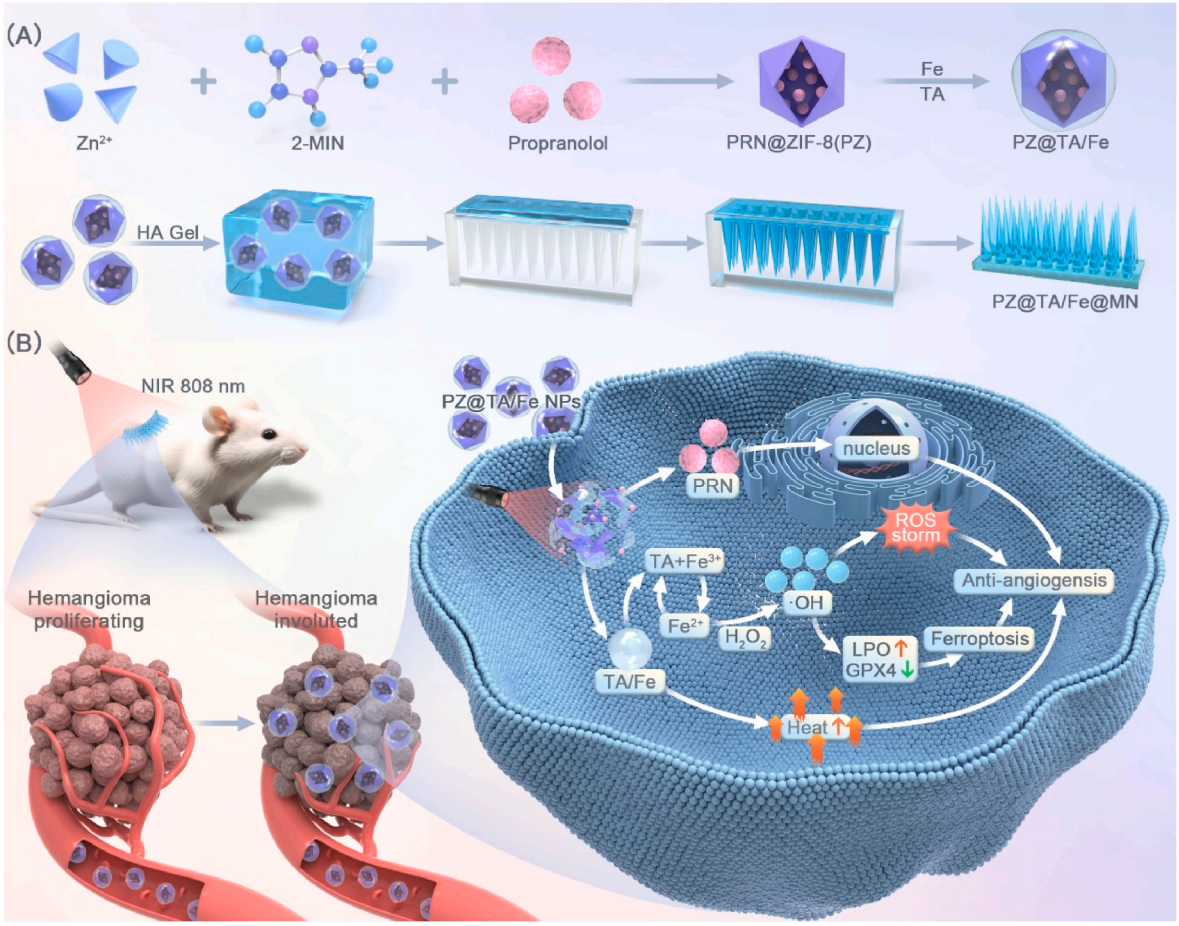

Scheme 1. (A) Synthesis process of PZ@TA/Fe@MNs. (B) Schematic illustration of PZ@TA/Fe@MNs to combine photothermal therapy with ferroptosis therapy in hemangiomas treatment.

TA/Fe nanocomplexes to possess photothermal responsiveness. These photothermal nanoparticles were then prepared within hyaluronic acid (HA) gel to create dissolving MNs patch. The MNs degraded in vivo and released PZ@TA/Fe NPs. The PZ@TA/Fe NPs could induce ferroptosis and combine with photothermal therapy, providing a superior anti-angiogenic effect. Additionally, this approach enhanced the accumulation of therapeutic drugs at the lesion site, addressed the low transdermal efficiency and potential issues of pain and scarring associated with traditional drug delivery methods, improved drug absorption rates, prolonged the duration of drug action, and reduced adverse side effects. To the best of our knowledge, this is the first study to utilize ferroptosis in hemangioma treatment and propose a microneedle nanoplatform combining PTT with ferroptosis therapy to exert anti-angiogenic effect, showing potential as a novel method for hemangioma therapy or adjuvant hemangioma therapy.

2. Materials and methods

2.1. Materials

2-methylimidazole(2-MIM), tannic acid and ferrous chloride ($FeCl_2 \bullet 4H_2O$) were obtained from Macklin Biochemical (Shanghai, China). Zinc nitrate hexahydrate ($Zn(NO_3)_2 \bullet 6H_2O$) was purchased from Aike Chemical Technology (Zhejiang China). Hyaluronic acid was obtained from Bloomage Biotechnology (Shandong, China), and 8-arm-PEG-OH (40 kDa) was purchased from SinopegBiotech (Fujian, China). Propranolol (PRN) was purchased from Solarbio (Beijing, China). The antibodies include: anti-GLUT1 (Proteintech, 21829-1-AP), anti-GPX4 (ABclonal, A21440), anti-VEGF (Proteintech,19003-1-AP), anti-CD31 (Proteintech,3F8E2).

2.2. Preparation of TA/Fe nanocomplexes

Ferrous chloride ($FeCl_2 \bullet 4H_2O$, 20 mg) was dissolved in double distilled water (4 mL) and stirred vigorously for 5 min. Tannic acid (TA, 10 mg) was dissolved in double distilled water (4 mL) and then dropwise added to the above solution, followed by stirring. The obtained TA/Fe nanocomplexes were centrifuged, purified, filtrated and finally stored at 4 °C for further use.

2.3. Preparation of PRN@ZIF-8 and PRN@ZIF-8@TA/Fe NPs

For preparation of PRN@ZIF-8@TA/Fe (PZ) NPs, PRN (50 mg) were first completely dissolved in water (200 μL), and added to 2 mL Zn $(NO_3)_2 \bullet 6H_2O$ solution (40 mM) with vigorous stirring. Consequently, a mixture of 2-methylimidazole (160 mM) and 8-arm-PEG-OH (10 mg) was added to 2 mL of water and then dropwise added in above solution. The mixture stirred vigorously for 1 h and white precipitates were gradually formed. The product was obtained by centrifugation (10000 rpm, 5 min) and washed with water for three times. The final PZ NPs were quickly merged and dissolved in TA/Fe nanocomplexes solution (500 μg/mL,2 mL), and then centrifugated to obtain the black precipitates product. The PZ@TA/Fe NPs were washed with water for three times and obtained the final production. The NPs were both stored at 4 °C for further study.

2.4. Particle characterization

The morphology of PZ and PZ@TA/Fe NPs were analyzed using transmission electron microscopy (TEM, model JEM-1400 by JEOL, Japan) and scanning electron microscopy (SEM, model G300 by Zeiss, Germany). To prepare the samples for TEM and SEM measurements, 1 μL of particle suspension was deposited on a silicon wafer or a copper grid and then followed by air dry. The zeta potential and hydrodynamic size of the NPs were measured by Malvern Zetasizer (Nano ZS90, UK). The crystal structure was measured by powder X-ray diffraction (XRD, D8 focus, Germany).

2.5. In vitro drug release

A dispersion of PZ@TA/Fe NP (1 mg/mL) was placed into a dialysis bag (Thermo Scientific, MWCO 3500) and dialyzed against with 40 mL of phosphate buffer (10 mM) at pH 7.4 or 5.5 under constant stirring. At specified time intervals, 500 μL samples were extracted from the buffer and analyzed using an ultraviolet–visible (UV–vis) spectrophotometer (model UV2600, Shimadzu, Japan) to evaluate PRN concentration. The absorbance at 290 nm was recorded to construct the standard curve.

2.6. Preparation of Alexa Fluor (AF488) labeled NPs

First, Alexa Fluor 488(AF488) dye was dissolved by DMOS. The PZ@TA/Fe NPs were incubated with the AF488 dye for 1 h in the dark to facilitate labeling. Following incubation, the AF488 labeled NPs were finally collected by centrifugation (10000 rpm, 5 min). The labeled NPs were then washed three times with water to ensure purity.

2.7. Cell cytotoxicity assay

HemECs were seeded in 96-well plates at a density of 5×10^3 cells per well for 24 h and then cells were incubated with different culture medium. The 808 nm NIR laser was applied for HemECs treated with PZ@TA/Fe NPs. The cells were continued to culture for 24 h. CCK-8 solution (Tongren, Shanghai, China) was added to each well and incubated for 1h. The absorbance was measured at 450 nm using a microplate reader (Thermo Fisher, Shanghai, China).

2.8. Calcein-AM/PI staining assay

HemECs were seeded in 24-well plates at a density of 1×10^4 cells per well and cultured for 24 h, then the cells were treated with different solution for 12 h and applied 808 nm NIR laser. The medium was discarded and the cells were washed with PBS 3 times. Fresh medium was added, including calcein AM and PI, and incubated at 37 °C in the dark for 30 min. Finally, the cells were observed by inverted fluorescence microscope.

2.9. Cell migration assays

Cell migration assays were conducted using 24-well transwell plate (Costar, No. 3422, 8 μm pore size). HemECs were pretreated with different culture medium for 12 h, and then HemECs were seeded in the upper chamber at 2×10^4 cells per well and cultured in serum-free ECM. The bottom chamber was filled ECM with 10 % FBS. After 24 h incubation, HemECs had successfully migrated through the membrane and were fixed and stained. The samples were documented through photography.

2.10. Ethynyl-2-deoxyuridine (EdU) assay

Cell proliferation ability was assessed using the ethynyl-2-deoxyuridine (EdU) Apollo DNA kit (RiboBio, Guangzhou, China). HemECs were seeded in 96-well plates at a density of 3×10^3 cells per well and treated with specific medium for 24 h. EdU (20 μM) was added to per well and incubated at 37 °C for 2 h. Then, HemECs were stained with Apollo 567 and Hoechst 33342 following the manufacturer's instructions and observed via inverted fluorescence microscopy at dark.

2.11. Reactive oxygen species (ROS) staining assay

HemECs were seeded in 24-well plates at a density of 1×10^4 cells per well and incubated with specific culture medium for 24 h. NIR laser applied for HemECs treated with PZ@TA/Fe NPs. Afterward, the cells were treated with DCFH-DA (Beyotime, Shanghai, China) at a concentration of 10 μM and incubated for 30 min at 37 °C. Following incubation, the cells were washed with PBS for three times and then observed by an inverted fluorescence microscope.

2.12. BODIPY581/591-C11 fluorescent probe assay

HemECs were seeded in 24-well plates at a density of 1×10^4 cells per well, the different treatments were stimulated for 24 h. Then, the HemECs were incubated with 10 μm BODIPY581/591-C11 fluorescent probe(Thermo Fisher, Shanghai, China) for 30 min. The cells were washed with PBS for three times. The fluorescent probe staining was detected by an inverted fluorescence microscope.

2.13. Immunofluorescence assay

HemECs were treated with different media for 24 h to detect ferroptosis process. The samples were fixed with 4 % formaldehyde and incubated with goat serum for 1 h. HemECs and primary antibodies were incubated at 4 °C overnight. Then, HemECs were incubated with FITC-conjugated goat anti-rabbit IgG and cy3-conjugated goat anti-mouse IgG for 1 h at room temperature. Immunofluorescence staining was observed by confocal laser scanning microscopy (Leica, Germany).

2.14. Preparation of PZ@TA/Fe@MNs

The tip-loaded HA microneedles were fabricated via two-casting method. Firstly, the PZ @TA/Fe NPs (5 mg) was dissolved in 20 mL water and mixed with HA (10 mg). The NPs-loaded HA solution was stirred vigorously and defoamed by centrifugation (3000 rpm, 5min). The NPs-loaded HA solution was poured into each PDMS mold and then placed in 50 mL centrifugal tube \ containing PDMS inserts. After that, they were centrifuged (3000 rpm, 5min) repeatedly until the tips of microneedles was filled completely. Superfluous solution left on the surface of PDMS molds was removed. Then, the pure HA gel solution (10 wt%) was added to the surface of the molds to form the base of microneedles. These fabricated molds were dried in an oven overnight at 30 °C. Finally, the PZ@TA/Fe NPs loaded HA microneedle patches were separated from the molds carefully and stored in the dry and dark environment for further use. The PZ-loaded HA microneedle patches were prepared by the same production process.

2.15. Animal studies

All experimental procedures were approved by the Research Ethics Committee of Shandong Provincial Hospital Affiliated with Shandong First Medical University (Shandong, China). BALB/c male mice (5 weeks old) were obtained from Beijing Vital River Laboratory Animal Technology. HemECs and HUVEC were used to establish hemangioma models. HemECs (1×10^6) and HUVEC (5×10^5) were loaded in 200 μL of matrigel (BD, SanJose, CA) and then injected into the right posterior side of the hind leg of the mice. When the tumor color converted red, the treatment began. The mice were randomly divided into six groups: Control, PRN Gel, HA MNs, PZ@MNs, PZ@TA/Fe@MNs, PZ@TA/Fe@MNs + Laser. The microneedle therapy continued every other day for two weeks. The NIR laser (1.5 W cm^{-2}) continued for 10 min at

tumor site after applying PZ@TA/Fe MNs. The vascular information was monitored by Visual sonic VEVO 2100 (Fujifilm, Canda). After 2 weeks, all mice were sacrificed, and hemangioma models and major organs were dissected for further examination.

2.16. Statistical analysis

All data are presented as the mean ± standard deviation (SD). All data on significant differences were evaluated using a two-tailed

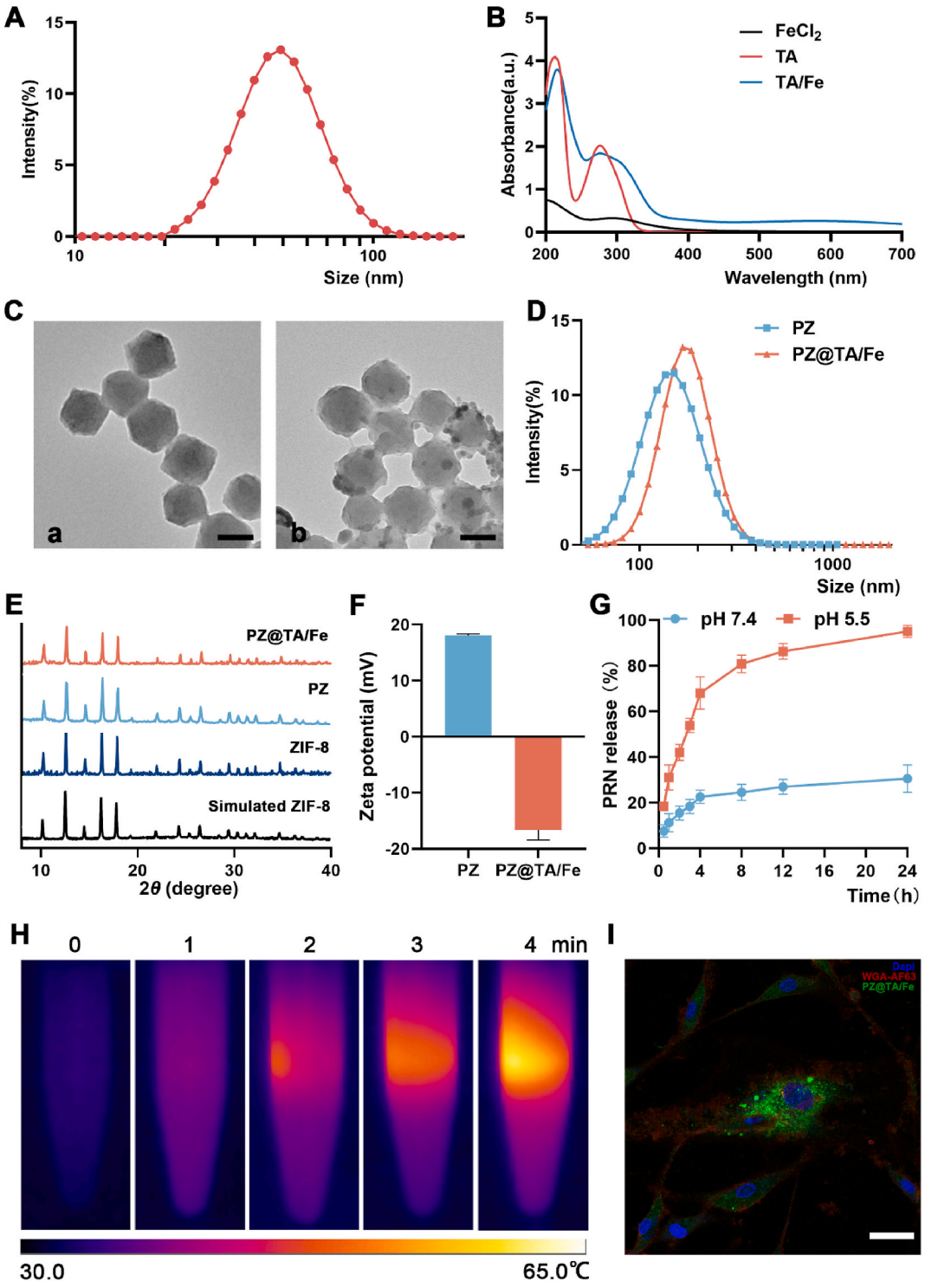

Fig. 1. Synthesis and characterization of PZ@TA/Fe NPs
(A) The size distribution of TA/Fe nanocomplexes; (B) UV–vis spectra of $FeCl_2$, TA and TA/Fe nanocomplexes; (C) The TEM images of PZ and PZ@TA/Fe NPs, (a):PZ, (b):PZ@TA/Fe NPs, scale bars for all images are 100 nm; (D) Hydrodynamic diameter distribution of PZ and PZ@TA/Fe NPs; (E) XRD pattern of different NPs; (F) The zeta potential of PZ and PZ@TA/Fe NPs; (G) The release of PRN from PZ@TA/Fe NPs under different pH conditions; (H) The photothermal effect of PZ@TA/Fe NPs under 808 nm laser irradiation; (I) Endocytosis of HemECs after incubation with PZ@TA/Fe NPs for 12 h, blue: Dapi, red: WGA-AF633, green: PZ@TA/Fe NPs labeled by AF488. Scale bars for all images are 20 μm. (For interpretation of the references to color in this figure legend, the reader is referred to the Web version of this article.)

Student's *t*-test and one-way analysis of variance (ANOVA). GraphPad Prism 9 (GraphPad Software) was utilized for statistical analysis. *p < 0.05, **p < 0.01 and ***p < 0.001 were considered.

3. Results and discussions

3.1. Synthesis and characterization of PZ@TA/Fe NPs

Firstly, TA/Fe nanocomplexes were fabricated via the coordination between TA and Fe (II). TA solution was added to $FeCl_2$ with a molar ratio of 1:1.6 (MTA: MFe) and the color of the solution changed into dark purple immediately. We also removed the precipitates from the solution by centrifugation and filtration. The hydrodynamic diameter, as determined by dynamic light scattering (DLS), was 54.6 nm (Fig. 1A). The UV–vis spectra results exhibited that LMCT band of TA/Fe nanocomplexes existed at 570 nm compared with TA and Fe(II) solution, indicating that there was a coordination interaction effect between Fe (II)and TA (Fig. 1B).

The PRN@ZIF-8(PZ) NPs were prepared via a one-pot synthesis step. In this process, poly(ethylene glycol) (PEG) was added as the mineralizer to improve stability and dispersity of ZIF-8 NPs. Then, PZ NPs were coated with TA/Fe shells by adsorption effect to obtain final PZ@TA/Fe NPs possessing photothermal effect. TEM was utilized to observe size and morphology of the PZ and PZ@TA/Fe NPs (Fig. 1C). The TEM images exhibited that PZ with hexagonal configuration had a similar morphology to ZIF-8 NPs and the size of PZ was approximately 155 nm, indicating that PRN exerted no significant effect on morphology of ZIF-8 NPs. PZ@TA/Fe NPs possessed a spherical configuration, and the particle size distribution was 170 nm. Compared with PZ NPs, PZ@TA/Fe NPs with TA/Fe nanocomplexes had an evident core–shell structure, demonstrating that TA/Fe nanocomplexes were successfully cloaked in the surface of PZ NPs (Fig. 1C). Moreover, these NPs both possessed good dispersibility. Furthermore, DLS was used to measure the size of PZ and PZ@TA/Fe NPs. These results demonstrated that the size of PZ and PZ@TA/Fe NPs were respectively 150 nm and 185 nm, which were almost similar with the microscopic observations (Fig. 1D). Powder X-ray diffraction (XRD) measurements were conducted to evaluate the crystal structures of ZIF-8 and drug-loaded ZIF-8 NPs. The results showed that the diffraction peaks of simulated ZIF-8 NPs, ZIF-8 NPs and drug-loaded ZIF-8 NPs were almost similar. This similarity indicated that the encapsulation of drugs and TA/Fe surface modification did not alter the crystal structure of the ZIF-8 NPs (Fig. 1E). The zeta potentials of PZ and PZ@TA/Fe NPs were also measured to confirm the coating. The TA/Fe surface modification changed the surface zeta from +18 mV potential to −16.5 mV (Fig. 1F). When Zn^{2+} and 2-MIM are combined in a solution, numerous Zn^{2+} ions coordinated at the surface of the PZ NPs, resulting in a positive charge. The phenolic groups in TA, being negatively deprotonated, could interact with the positively charged Zn^{2+}, which aided in the growth of the TA/Fe film on the PZ surface and altered the zeta potential. The encapsulation of PRN was quantified by UV–visible spectrophotometry (Fig. S1). There were approximately 101.8 μg of PRN in 1 mg of PZ@TA/Fe NPs, indicating ZIF-8 NPs had a good cargo loading efficiency. As an ideal drug delivery nanocarrier, the stability is a vital factor for medical application. The DLS results presented that the size of PZ@TA/Fe NPs were not changed substantially after incubation with culture medium with serum and culture medium without serum for five days (Fig. S2), demonstrating that these NPs possessed remarkable stability under physiological conditions and had the potential for long time biomedical research. Moreover, due to the hypoxia and abnormal tumor metabolic process, it is known that tumor microenvironment is more acidic compared with normal tissues [45]. Therefore, pH-responsive nanocarriers are particularly suitable for tumor therapy applications. To evaluate the performance under different pH conditions, PZ@TA/Fe NPs were incubated with PBS at pH levels of 5.5 and 7.4, simulating various physiological environments and the release of PRN was monitored at different time points. The results shown that the PBS buffer (pH 7.4) caused minimal PRN release, with only about 30 % PRN being released within 24 h. In contrast, under acidic conditions (pH 5.5), the NPs exhibited a significantly accelerated PRN release rate after just 8 h incubation, and eventually there was almost 95 % PRN released from the PZ@TA/Fe NPs (Fig. 1G). The accelerated and more efficient release of PRN at lower pH will be beneficial for the improved therapeutic efficacies in tumor sites. Additionally, this pH-responsive behavior could reduce the risk of drug leakage in normal tissues, thereby improving the safety and specificity of the treatment.

The photothermal potency of NPs used for PTT is an indispensable factor that guarantees the actual therapeutic efficacy. It has been widely reported that hyperthermia reaching 43 °C can start to cause tumor cells damage and apoptosis [46]. Hence, the photothermal properties of PZ@TA/Fe NPs were measured under the irradiation of an 808 nm laser (1.5 W/cm^{-2}) and the temperature was recorded by an infrared thermal camera (Fig. 1H). Compared with the ZIF-8 and PZ NPs, the PZ@TA/Fe NPs were able to rapidly increase the temperature up to 60 °C upon irradiation, thus demonstrating the superior photothermal effect of the TA/Fe nanocomplexes coating (Fig. S3). In addition, by varying the concentration of PZ@TA/Fe NPs, irradiation time, or power density, the temperature elevation level could be precisely controlled (Figs. S4 and S5). These results suggested that the temperature of PZ@TA/Fe NPs could be accurately regulated through multiple feasible methods, making it possible to adjust heating effect in a manner dependent on the concentration of the NPs, laser power or irradiation time.

In addition, to monitor the endocytosis of PZ@TA/Fe NPs in HemECs, the PZ@TA/Fe NPs were labeled with Alexa Fluor 488 dye. The fluorescence intensity of HemECs began to increase after almost 4 h incubation, and the fluorescence intensity of HemECs strengthened gradually as the time progressed, indicating that an increased uptake of PZ@TA/Fe NPs in cells (Fig. I, S6). The quantitative analysis of the mean fluorescence intensity (MFI) also revealed that more NPs were internalized by cells in the process of time (Fig. S7). Above all, we successfully prepared the PZ@TA/Fe NPs. These NPs possessed several advantageous characteristics, including suitable size, pH responsiveness, stability, and adjustable photothermal effect.

3.2. The performance and anti-angiogenic effect of PZ@TA/Fe NPs in vitro

The CCK-8 assay was first performed on HemECs to evaluate the toxicity of different treatments. Initially, the focus was on assessing the biocompatibility of ZIF-8 NPs with HemECs. The results demonstrated that ZIF-8 NPs exhibited minimal cytotoxicity at concentrations up to 60 μg/ml (Fig. 2A), indicating the outstanding biocompatibility and low cytotoxicity of the ZIF-8 NPs. To ensure safety and decrease potential toxicity of nanocarriers, the concentration of ZIF-8 NPs used in our experiments was maintained below 60 μg/ml. In this concentration, ZIF-8 NPs assisted in optimizing the therapeutic efficacy of nanodrugs while minimizing undesirable side effects. Due to the EPR effect, the nanodrugs could accumulate more in tumor sites and cells. The ZIF-8 NPs and TA/Fe shell degraded in tumor cells under the acidic microenvironment to release the encapsulated PRN and Fe (II). The upregulated Fe (II) levels would augment the effects of ferroptosis. Accordingly, compared with PZ NPs, the PZ@TA/Fe NPs exhibited better apoptotic effect under similar concentration of PRN. Upon 808 nm NIR irradiation, with the increase of concentration of the nanodrugs, the temperature elevated and directly caused damage and inhibition to HemECs, thereby resulting in the maximum cytotoxicity (Fig. 2B). Next, the cell killing effect was further observed by calcein-AM/PI staining. In this assay, calcein AM selectively stains live cells, emitting green fluorescence, while propidium iodide (PI) labels dead cells, producing red fluorescence. Under identical PRN concentration, the PZ@TA/Fe NPs with 808 nm laser irradiation showed the highest percentage of dead cells, exhibiting maximum proportion of red fluorescence, which indicated distinct

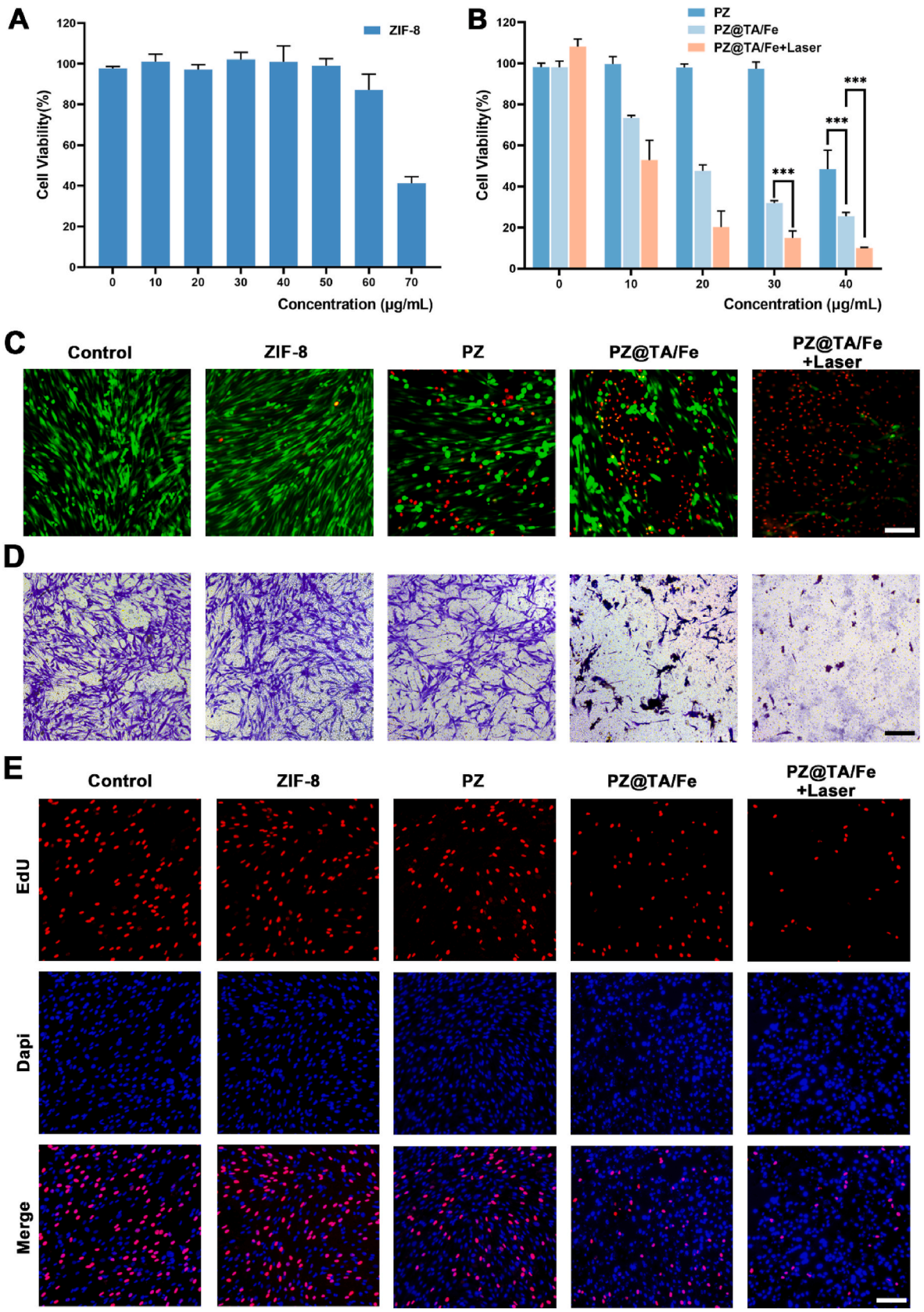

Fig. 2. The performance and anti-angiogenesis effect of PZ@TA/Fe NPs in vitro
(A) The cytotoxicity of ZIF-8 NPs to HemECs (n = 5 each); (B) The cytotoxicity of different treatments to HemECs (n = 5 each); (C) Calcein-AM/PI staining to detect apoptosis in different treatments; (D) Transwell assay detection to assess cell migration inhibition in different treatments; (E) The EdU assay was performed to assess proliferative cells, scale bars for all images are 100 μm.

cytotoxicity to HemECs (Fig. 2C,S8). These results also indicated PZ@TA/Fe NPs had outstanding photothermal effect and photothermal conversion efficiency, leading to cell death and enhancing therapeutic efficacy. To further evaluate the inhibition of cell invasion and migration, transwell assays were conducted. The transwell assays result showed that a notable reduction in the migration of HemECs following treatment (Fig. 2D). The PZ@TA/Fe NPs treatment under laser irradiation exhibited the most evident cell migrating inhibition phenomenon.

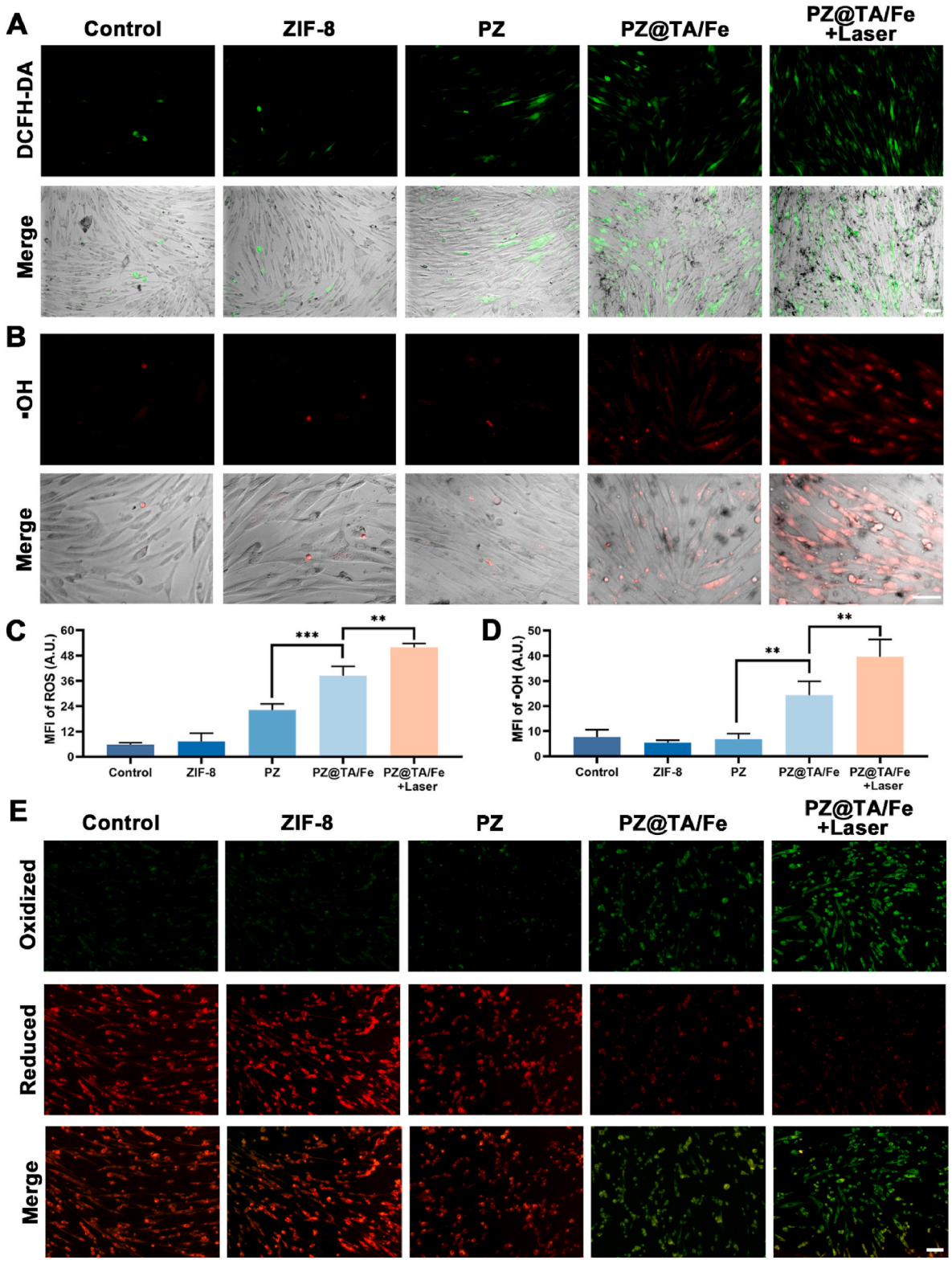

Fig. 3. Mechanism of Ferroptosis induced by PZ@TA/Fe NPs.
(A)DCFH-DA probe to detect ROS generation of HemECs with different treatments; (B) Fluorescent images to detect ·•OH levels with different treatments; (C) Mean fluorescence intensity (MFI) to compare ROS levels; (D) MFI to compare •OH levels; (E) BODIPY581/591-C11 fluorescent probe to assess the accumulation of LPO in cells with different treatments, scale bars for all images are 100 μm.

Quantitative analysis demonstrated that the migration cells decreased approximately 90 % in PZ@TA/Fe with laser irradiation group (Fig. S9). This decrease indicated the effectiveness of the intervention in suppressing mobility of HemECs. As migration is a key factor in the process of cellular invasion, these results suggested a potential therapeutic benefit in conditions where the control of cell spread is crucial. The tube formation assay was utilized to assess the anti-angiogenic effect under different treatments. The PZ treatments exhibited dense, intact vascular-like network, exhibiting a typical angiogenic phenotype. In PZ@TA/Fe treatment, the vascular network significantly reduced, with evident structural fragmentation, indicating that PZ@TA/Fe treatment effectively inhibited angiogenesis. Importantly, the PZ@TA/Fe under laser treatment showed the most evident angiogenic inhibitory effect. The vascular network was nearly completely disrupted, with only scattered cells and no intact structures (Fig. S10). In addition, the anti-proliferative impact was explored, the proliferating cells were marked with red fluorescence of EdU. After treatment with PZ NPs, there were still a considerable number of cells presenting intact proliferative potential; however, only sparse red fluorescence was observed in tumor cells treated with the PZ@TA/Fe NPs with laser irradiation (Fig. 2E). The proportion of proliferating cells dropped approximately 30 % according to quantitative fluorescence analysis (Fig. S11).

Taken together, we established the PZ@TA/Fe NPs with reliable photothermal conversion efficiency, the NPs under 808 nm laser irradiation presented the best apoptotic effect against the HemECs and obviously inhibited invasion, migration, proliferation ability of HemECs, indicating that PTT and ferroptosis could exhibit synergetic effect.

3.3. Mechanism of Ferroptosis induced by PZ@TA/Fe NPs

To assess the underlying mechanism of PZ@TA/Fe in anti-angiogenesis to treat hemangioma, the level of reactive oxygen species (ROS), a marker of oxidative stress, was first measured. PTT has the capability to elevate ROS levels in HemECs. Moreover, Fe (III) could react with TA to form Fe (II), which subsequently utilized H_2O_2 to generate excessive hydroxyl radical and oxygen radical through Fenton reaction, eventually leading to an evident accumulation of ROS. Intracellular ROS level was evaluated using a ROS-sensitive fluorescent probe. Minimal green fluorescence was observed in groups treated with PZ NPs, and only mild green fluorescence was observed in PZ@TA/Fe NPs treatment group, attributable to the release of Fe (II) induced by ferroptosis. In contrast, strong green fluorescence was visualized in PZ@TA/Fe NPs + Laser group due to effective photothermal conversion efficiency of TA/Fe surface modification to accelerate ROS generation (Fig. 3A). The level of ROS generated by different treatments in cells was also quantified (Fig. 3C). This result demonstrated that the combination of PTT and ferroptosis treatment could synergistically induce a ROS storm, leading to cell damage. The hydroxyl radical (•OH), a key product of the Fenton reaction, was also measured. The control group, as well as the groups treated with ZIF-8 and PZ NPs, were merely unable to induce the Fenton reaction effectively, showing no significant accumulation of •OH. This lack of hydroxyl radical generation indicated that these treatments alone were insufficient to trigger the oxidative stress that was necessary for ferroptosis to eradicate HemECs. Conversely, the PZ@TA/Fe NPs with laser irradiation exhibited the most evident •OH generation phenomenon. The photothermal effect induced by laser irradiation on the TA/Fe surface may accelerate the Fenton reaction kinetics, leading to a higher yield of •OH. Meanwhile, PZ@TA/Fe NPs with high surface area and porous nature may provide more active sites for the Fenton reaction to occur (Fig. 3B). We quantified the level of •OH generated in different treatment groups as well (Fig. 3D).

Ferroptosis is characterized by the accumulation of lipid peroxides (LPO), which can be distinguished from cell apoptosis [47]. LPO refers to lipids that contain peroxy group, when unsaturated fatty acid chains react with free radicals or ROS. Consequently, LPO serves as a crucial marker for ferroptosis [48]. To evaluate LPO levels, the BODIPY581/591-C11 fluorescent probe was implemented. In the reduced state, the cells have the green fluorescence, and upon oxidation in live cells, fluorescence shifts from red to green. The green fluorescence of HemECs incubated with PZ@TA/Fe NPs was significantly stronger than the cells incubated with ZIF-8 and PZ NPs, clearly supporting the presence of LPO in HemECs. Additionally, the laser irradiation could further boost the LPO generation and accumulation in cells, the PZ@TA/Fe NPs with laser irradiation displayed the most intense green fluorescence while the slightest red fluorescence, indicating the substantial concentration of LPO in cells to induce ferroptosis effectively (Fig. 3E). Glutathione peroxidase 4 (GPX4) plays a pivotal role in regulating ferroptosis by enzymatically reducing cytotoxic phospholipid hydroperoxides to non-toxic lipid alcohols, thereby maintaining membrane integrity and cellular redox homeostasis. Previous studies have demonstrated that GPX4 expression is frequently dysregulated in tumor cells undergoing ferroptosis, making it a critical biomarker for evaluating ferroptotic responses. Therefore, the immunofluorescence assay was used to investigate the expression of GPX4. The resulted showed that the PZ@TA/Fe NPs administration could downregulate expression of GPX4 to occur ferroptosis process. Combining with laser irradiation, the expression of GPX4 was reduced to lowest level. These results also proved that Fe (II) degraded from TA/Fe surface modification could occur ferroptosis (Fig. S12). Above all, PZ@TA/Fe NPs with laser irradiation could become a promising strategy for enhancing the efficacy of hemangioma therapy by utilizing the unique properties of ferroptosis-inducing agents along with photothermal therapy. This combined approach not only targeted angiogenesis phenomenon but also exploited the vulnerability of HemECs to oxidative stress.

3.4. Synthesis and characterization of PZ@TA/Fe@MNs in vitro

As for the dissolving MNs patch, the microneedle structure gradually dissolved and degraded upon insertion into the skin, simultaneously releasing therapeutic agents. Hence, it is critical for MNs patch to possess good biodegradability and biosafety. Hyaluronic acid (HA), a natural polysaccharide, is abundant in the extracellular matrix. HA possesses characteristics such as biocompatibility, biodegradability, non-immunogenicity, and non-toxicity. Based on that, HA is an ideal material for the fabrication of MNs patch [49]. We utilized HA as the component of MNs patch. We merged HA gels with PZ@TA/Fe NPs, and then made them fill in the microneedle mold by centrifugation and vacuum suction. The base layer of the MNs patch was composed of pure HA gels to prevent superficial skin damage caused by the photothermal effect of the PZ@TA/Fe NPs. The MNs was dried overnight and could be easily peeled off from the mold (Fig. 4A). The needle tips exhibited black color resulting from the content of PZ@TA/Fe NPs (Fig. 4B). The patch was square with 14.5 mm side length and a 15 × 15 tapered tip array on it. The needle structures were neatly arranged on the patch, and the arrays of patch were uniformly distributed. The SEM images revealed that the needle structure was conical, and dimensions of the fabricated arrays were about 1000 μm in height and 350 μm in width at the base (Fig. 4C and D). The fabricated PZ@TA/Fe@MNs possessed enough mechanical strength to puncture skin (Fig. 4E). The photothermal effect of the MNs patch in response to NIR light was also evaluated. Compared with pure HA MNs and PZ@MNs, the temperature of PZ@TA/Fe@MNs upon laser irradiation could reach approximately 60 °C rapidly, demonstrating the excellent photothermal properties and high photothermal conversion efficiency of PZ@TA/Fe NPs (Fig. 4F and G). For evaluating the photothermal conversion stability of PZ@TA/Fe@MNs, a predetermined on/off cycle of NIR light was exposed to the MNs patch. It was found that the temperature of MNs patch elevated rapidly to a peak upon NIR triggering and dropped to room temperature immediately after removing the NIR irradiation. The cyclical irradiations had no evident impact on the peak temperature, indicating the conspicuous photothermal stability of PZ@TA/Fe@MNs (Fig. 4H). These results highlighted the superior mechanical and photothermal properties of the

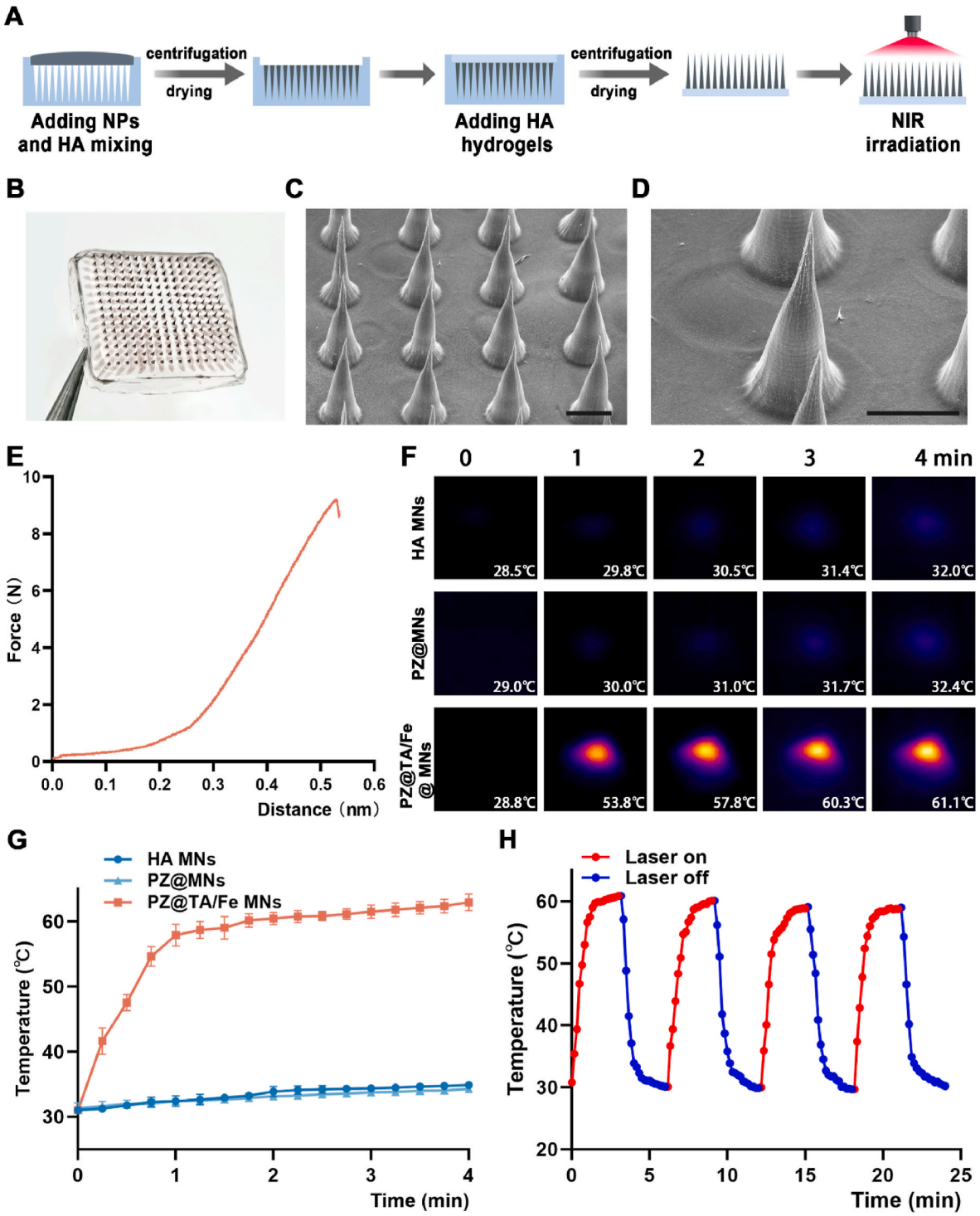

Fig. 4. Synthesis and characterization of PZ@TA/Fe@MNs in vitro
(A) Preparation procedure of PZ@TA/Fe@MNs; (B) Gross appearance of PZ@TA/Fe@MNs; (C, D) SEM images of the prepared PZ@TA/Fe@MNs pathch, scale bars for all images are 500 μm. (E) Mechanical performance of PZ@TA/Fe@MNs; (F) Photothermal images of HA MNs, PZ@MNs and PZ@TA/Fe@MNs under 808 nm NIR laser irradiation; (G) The time-temperature curves of HA MNs, PZ@MNs and PZ@TA/Fe@MNs; (H) The time-temperature curve of PZ@TA/Fe@MNs under repeated laser "on/off" cycles irradiation.

PZ@TA/Fe@MNs, which could be considered as a promising tool for targeted and efficient transdermal drug delivery.

3.5. The characterization of PZ@TA/Fe@MNs in vivo

The penetration strength and capacity are essential for the application of MNs in vivo. The PZ@TA/Fe@MNs were pressed on the skin of mice. H&E staining presented that MNs could create microchannels in the skin with no visible skin irritation, indicating that the MNs structure possessed sufficient mechanical strength to penetrate through the stratum corneum into the dermis (Fig. 5A). Moreover, the potential skin damage caused by MNs was detected. As for a novel transdermal drug delivery method, the MNs patch should result in minimal damage to skin, which can increase the potential for long-term drug delivery and

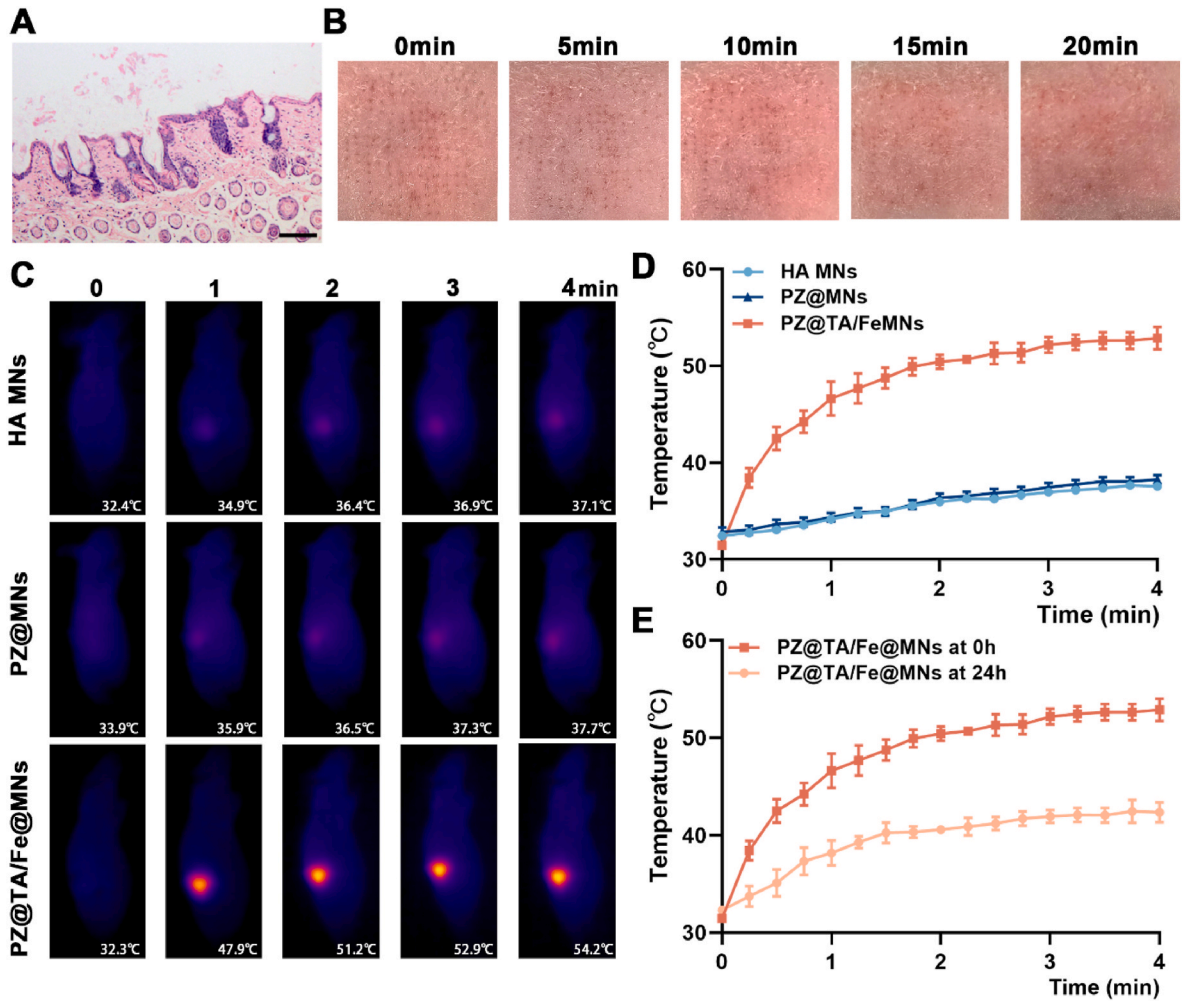

Fig. 5. The characterization of PZ@TA/Fe@MNs in vivo.
(A)The H&E staining of MNs patch penetrating into mice skin, scale bars for all images are 100 μm; (B) The recovery images of microchannels created by PZ@TA/Fe@MNs in vivo; (C) Photothermal images of HA MNs, PZ@MNs and PZ@TA/Fe@MNs in vivo under 808 nm NIR laser irradiation; (D) The time-temperature curve of HA MNs, PZ@MNs and PZ@TA/Fe@MNs in vivo under 808 nm laser irradiation; (E) The time-temperature curves of PZ@TA/Fe@MNs under 808 nm laser irradiation immediately and after 24 h in vivo.

enhance patient compliance. Hence, the recovery images of microchannels created by MNs on the mice skin were recorded. The puncture marks gradually diminished and completely disappeared after approximately 20 min, confirming minimal invasiveness of the MNs to skin (Fig. 5B). For delivering therapeutic agents into the lesion area, the solubility of MNs was important. After being pressed into mice skin for 20 min, the needle tips could be rapidly dissolved, leaving only the basal part of MNs patch, which proved efficient dissolution and subsequent release of the therapeutic agents into target area (Fig. S13). The photothermal effect of PZ@TA/Fe@MNs in vivo was also evaluated. The PZ@TA/Fe@MNs inserted in tumor sites were exposed to NIR laser irradiation. The temperature of PZ@TA/Fe@MNs increased rapidly to 52 and 56 °C (Fig. 5C and D). It should be noted that the formation and development of blood vessels, as well as the damage and apoptosis of tumor cells, can be inhibited at a local temperature of approximately 53 °C without causing permanent burn damage [50]. Hence, PZ@TA/Fe@MNs could generate appropriate photothermal effect to exert therapeutic effect. The PZ@TA/Fe@MNs in vivo also possessed photothermal conversion stability, and the on/off cycle of NIR light did not significantly alter the peak temperature (Fig. S14). The MNs administration was also simulated, the temperature of PZ@TA/Fe@MNs sticking to lesion area was obviously decreased after 24 h, suggesting proper dissolving properties of PZ@TA/Fe@MNs (Fig. 5E).

3.6. Inhibitory effect of PZ@TA/Fe@MNs in vivo

Subsequently, we evaluated the anti-angiogenic effect in nude mouse with hemangioma models. The HemECs and HUVECs were mixed in Matrigel and injected into the flanks of the mice to establish hemangioma models (Fig. 6A). After two weeks, the color of hemangioma modes turned red, indicating formation of vascular structure. To further confirm the successful establishment of hemangioma models, the unique immunohistochemical markers, glucose transporter 1 (GLUT1) and CD31, were used to label the hemangioma tissue. The results showed that GLUT1 and CD31 were expressed abundantly in hemangioma models, substantiating the development of the vascular structures and the establishment of hemangioma models successfully (Fig. 6B). Then, the mice were randomly divided into 6 groups: 1) Control, 2) PRN gel, 3) HA MNs, 4) PZ@MNs, 5) PZ@TA/Fe@MNs, and 6) PZ@TA/Fe@MNs + Laser, and the treatments were started. Significantly, the commercial PRN gel, widely used in clinic, was also utilized to compare the efficiency of transdermal drug delivery with MNs. The efficacy of anti-angiogenic treatment was first assessed based on changes in lesion color, which is the most apparent predictive indicator. The control, PRN gel, and HA MNs group presented almost same dark color of hemangioma xenografts, demonstrating the abundant vascular formation and progression in hemangioma. Due to the low penetration ability and

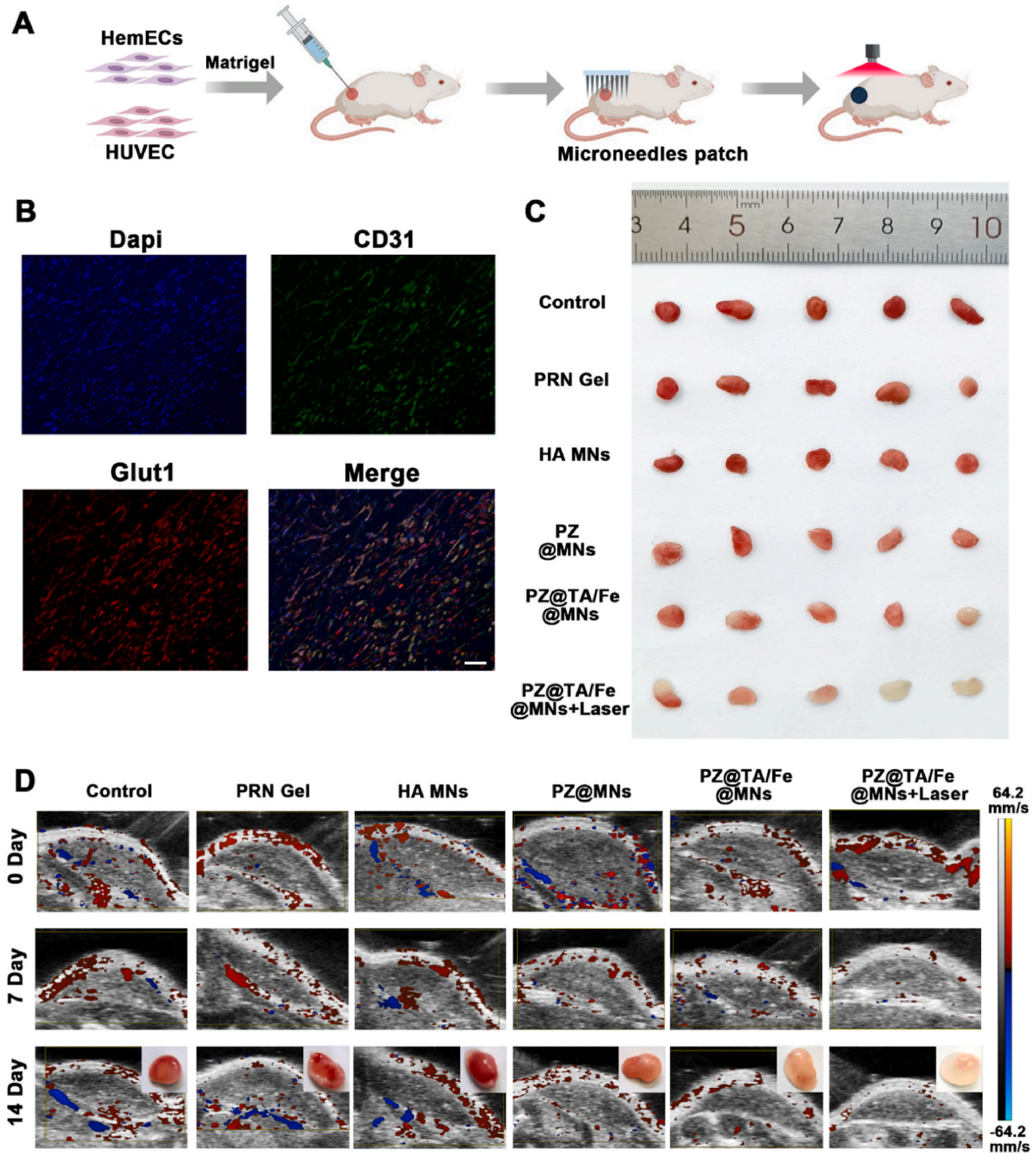

Fig. 6. Inhibitory effect of PZ@TA/Fe@MNs in vivo.
(A) Schematic illustration of hemangioma model in MNs therapy; (B)The immunofluorescence staining of resected hemangioma model, scale bars for all images are 20 μm; (C) Photograph of resected hemangioma model after different treatments; (D) The blood flow information during MNs therapy observed by color doppler ultrasound, red signal: blood flows closer to the ultrasound probe, blue signal: blood flows away from the ultrasound probe. (For interpretation of the references to color in this figure legend, the reader is referred to the Web version of this article.)

tendency to be easily removed, the PRN gel treatment did not show obvious therapeutic effects to the superficial treatment. Compared with PRN Gel, the PZ encapsulated in MNs could attain the sustainably release of therapeutic agents in situ, exhibiting the slightly shallower color. In contrast, the most distinct vascular involution was observed in the PZ@TA/Fe@MNs + Laser group, in which the hemangioma color almost completely disappeared (Fig. 6C). More importantly, to monitor the blood flow visually in hemangioma, the color doppler ultrasound was utilized to detect the anti-angiogenic effect during treatment. Color doppler ultrasound could obtain real-time imaging and realize the dynamic observation of blood flow. The blood flow maintained abundant in control, PRN gel, and HA MNs group and exhibited no evident decrease tendency. The PZ@MNs and PZ@TA/Fe@MNs group displayed decreased blood flow phenomenon, which indicated the MNs patch could exert better vascular inhibition effect. The blood flow signal of PZ@TA/Fe@MNs + Laser treatment group began to decrease during therapy period and almost disappeared after treatment, demonstrating PZ@TA/Fe@MNs upon NIR laser irradiation blocked novel vascular formation effectively and exerted best therapeutic effect (Fig. 6D). All results demonstrated that PTT induced by PZ@TA/Fe NPs released from the MNs patch could effectively damage the vascular structure and accelerated hemangioma involution.

To validate the antiangiogenic effect of different treatments, H&E staining was carried out (Fig. 7A). The microvessels density (MVD)

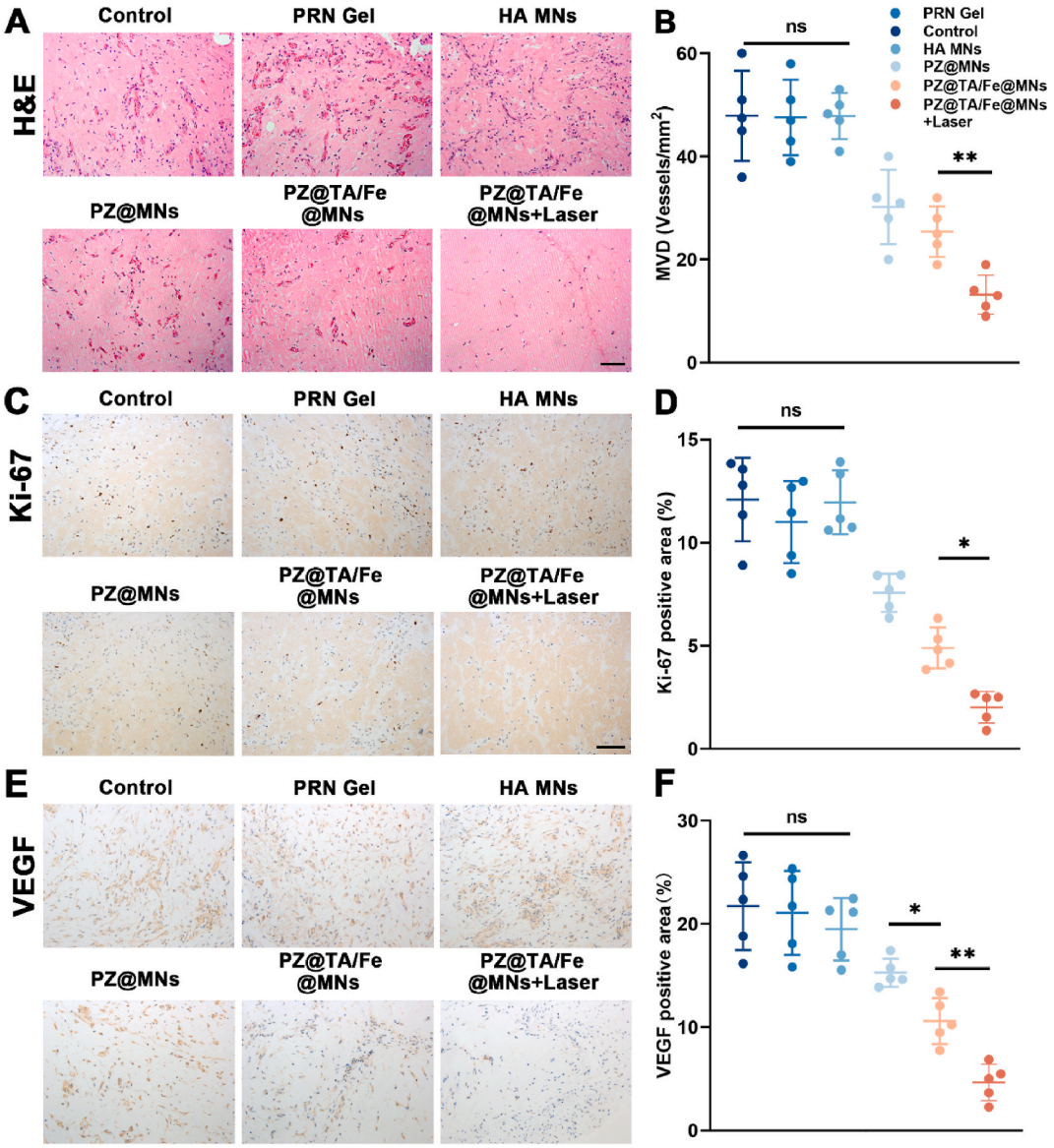

Fig. 7. Inhibitory effect of PZ@TA/Fe@MNs in vivo
(A) H&E staining of resected hemangioma model after different treatments; (B) Microvessel density (MVD) analysis in hemangioma model after different treatments; (C) Ki-67 immunohistochemistry staining of resected hemangioma model to detect anti-proliferative effect; (D)Positive area percentages of Ki-67 immunohistochemistry; (E) VEGF immunohistochemistry staining of resected hemangioma model to detect anti-angiogenic effect, scale bars for all images are 100 μm; (F)Positive area percentages of VEGF immunohistochemistry.

analysis revealed that applying MNs therapy led to fewer microvessels compared with other treatment groups. In addition, the MVD value was lowest in the group treated with PZ@TA/Fe@MNs in combination with laser therapy (Fig. 7B). Further investigation involved staining for the proliferative and angiogenic indices. The results of Ki-67 staining showed that the PZ@TA/Fe@MNs + Laser group markedly inhibited hemangioma proliferation compared to other treatments, which was consistent with the results of the EdU assay in vitro (Fig. 7C and D). Vascular endothelial growth factor (VEGF) plays a crucial role in the formation and growth of blood vessels. The PZ@TA/Fe@MNs + Laser group showed significantly lower levels of VEGF expression, indicating that this treatment could decrease cell migration and proliferation to inhibit hemangioma progression (Fig. 7E and F).

Finally, the nanomaterials biosafety is one of the major concerns in biomedical applications. The body weight during different treatments was recorded. The results showed that the body weight of mice had no significant fluctuation, suggesting the negligible toxicity and safety of MNs therapy (Fig. S15). The hemolysis assay revealed negligible hemolytic activity for both PZ and PZ@TA/Fe NPs (Fig. S16A). The hemolysis rates were consistently below 5 % (Fig. S16B), indicating that the nanodrugs possessed excellent hemocompatibility and biosafety, and had potential for in vivo applications. H&E staining experiments of major tissues (heart, liver, spleen, lung, and kidney) were also performed. The major organs exhibited no evident lesions or abnormalities in tissue morphology and cellular integrity in the different treatment groups, demonstrating that the MNs treatment had no obvious side effects on major organs (Fig. S17). Above all, all results indicated that PZ@TA/Fe MNs exerted distinct therapeutic effects to hemangiomas in vivo and systemic application was safe in vivo application.

4. Conclusion

In this study, we fabricated PZ@TA/Fe@MNs to treat hemangiomas. The PZ NPs were first prepared by a one-pot method using PEG as the

mineralizing agent, and TA/Fe nanocomplexes were then modified on the surface of PZ NPs by electrostatic adsorption. The PZ@TA/Fe NPs possessed good biocompatibility, high photothermal conversion efficiency, controllable photothermal effect, and effective anti-angiogenic ability. The PZ@TA/Fe NPs were loaded in the MNs patch and PZ@TA/Fe@MNs had sufficient mechanical strength, excellent photothermal effect, and good biosafety. The PZ@TA/Fe@MNs could release Fe (II), and TA assisted to sustain Fe in the reduced state. Fe (II) further induced Fenton reaction and converted abundant H_2O_2 to •OH, enhancing the accumulation of intracellular lipid peroxidation, ultimately resulting in ferroptosis to damage vasculature and inhibit new blood vessels formation and extension. More importantly, TA/Fe shell upon on 808 nm NIR laser irradiation not only enhanced temperature to damage cell or vasculature directly but also accelerated Fenton reaction or ferroptosis. The photothermal therapy and ferroptosis therapy exerted a synergetic role in hemangioma therapy. The MNs method attained targeted delivery to lesion areas and maximized the delivery rate of the therapeutic agents. Our works show that PZ@TA/Fe@MNs enable transdermal drug delivery to induce photothermal effect and ferroptosis for effective hemangioma therapy. We believe that the innovative concept of "Ferroptosis-mediated anti-angiogenic therapy" may hold significant potential for clinical applications in hemangioma treatment.

CRediT authorship contribution statement

Yiming Geng: Writing – original draft, Project administration, Methodology, Investigation. **Cancan Meng:** Visualization, Investigation. **Hanzhi Zhang:** Methodology, Data curation. **Chuan Ma:** Supervision, Resources. **Xiao Fu:** Writing – review & editing, Resources. **Haiwei Wu:** Writing – review & editing, Supervision, Resources, Conceptualization.

Funding

This work was supported by the National Natural Science Foundation of China (82470425, 22202120, 82201092) and Natural Science Foundation of Shandong Province (ZR2024MH115, ZR2021MH086). This work was supported by Shandong Province Health Science and Technology Young Innovation Team Project.

Declaration of competing interest

The authors declare that they have no known competing financial interests or personal relationships that could have appeared to influence the work reported in this paper.

Acknowledgements

Not applicable.

Appendix A. Supplementary data

Supplementary data to this article can be found online at https://doi.org/10.1016/j.mtbio.2025.101748.

Data availability

Data will be made available on request.

References

[1] S.A. Mansfield, R.F. Williams, I. Iacobas, Vascular tumors, Semin. Pediatr. Surg. 29 (2020) 150975.
[2] C. Leaute-Labreze, J.I. Harper, P.H. Hoeger, Infantile haemangioma, Lancet 390 (2017) 85–94.
[3] R. Goelz, C.F. Poets, Incidence and treatment of infantile haemangioma in preterm infants, Arch. Dis. Child. Fetal Neonatal Ed. 100 (2015) F85–F91.
[4] K.S. Pahl, T.W. McLean, Infantile hemangioma: a current review, J. Pediatr. Hematol. Oncol. 44 (2022) 31–39.
[5] A. Leung, J.M. Lam, K.F. Leong, K.L. Hon, Infantile hemangioma: an updated review, Curr. Pediatr. Rev. 17 (2021) 55–69.
[6] A. Holm, J.B. Mulliken, J. Bischoff, Infantile hemangioma: the common and enigmatic vascular tumor, J. Clin. Investig. 134 (2024).
[7] L.C. Chang, A.N. Haggstrom, B.A. Drolet, E. Baselga, S.L. Chamlin, M.C. Garzon, K. A. Horii, A.W. Lucky, A.J. Mancini, D.W. Metry, A.J. Nopper, I.J. Frieden, Growth characteristics of infantile hemangiomas: implications for management, Pediatrics 122 (2008) 360–367.
[8] M. Park, Infantile hemangioma: timely diagnosis and treatment, Clin Exp Pediatr 64 (2021) 573–574.
[9] D.F. Sebaratnam, B.A. Rodriguez, L.F. Wong, O. Wargon, Infantile hemangioma. Part 2: management, J. Am. Acad. Dermatol. 85 (2021) 1395–1404.
[10] J. Mayer, S. Intzes, V.S. Oza, F. Blei, How we approach hemangiomas in infants, Pediatr. Blood Cancer 69 (Suppl 3) (2022) e29077.
[11] K. Ziad, J. Badi, Z. Roaa, A.H. Emily, Laser treatment of infantile hemangioma, J. Cosmet. Dermatol. 22 (Suppl 2) (2023) 1–7.
[12] C. Leaute-Labreze, D.L.R.E. Dumas, T. Hubiche, F. Boralevi, J.B. Thambo, A. Taieb, Propranolol for severe hemangiomas of infancy, N. Engl. J. Med. 358 (2008) 2649–2651.
[13] W. Zhou, S. He, Y. Yang, D. Jian, X. Chen, J. Ding, Formulation, characterization and clinical evaluation of propranolol hydrochloride gel for transdermal treatment of superficial infantile hemangioma, Drug Dev. Ind. Pharm. 41 (2015) 1109–1119.
[14] M.N. Xu, M. Zhang, Y. Xu, M. Wang, S.M. Yuan, Individualized treatment for infantile hemangioma, J. Craniofac. Surg. 29 (2018) 1876–1879.
[15] M. Khan, A. Boyce, D. Prieto-Merino, A. Svensson, E. Wedgeworth, C. Flohr, The role of topical timolol in the treatment of infantile hemangiomas: a systematic review and meta-analysis, Acta Derm. Venereol. 97 (2017) 1167–1171.
[16] D. Jian, X. Chen, K. Babajee, J. Su, J. Li, X. Hu, H. Xie, J. Li, Adverse effects of propranolol treatment for infantile hemangiomas in China, J. Dermatol. Treat. 25 (2014) 388–390.
[17] D.O. Lewis, Side-effects of propranolol, Br. Med. J. 2 (1966) 588.
[18] J. Ananth, K.M. Lin, Propranolol in psychiatry. Therapeutic uses and side effects, Neuropsychobiology 15 (1986) 20–27.
[19] V. Phatale, K.K. Vaiphei, S. Jha, D. Patil, M. Agrawal, A. Alexander, Overcoming skin barriers through advanced transdermal drug delivery approaches, J. Contr. Release 351 (2022) 361–380.
[20] M.R. Prausnitz, R. Langer, Transdermal drug delivery, Nat. Biotechnol. 26 (2008) 1261–1268.
[21] S. Ruan, Y. Zhang, N. Feng, Microneedle-mediated transdermal nanodelivery systems: a review, Biomater. Sci. 9 (2021) 8065–8089.
[22] A.F. Nazary, L. Salimi, S. Saghati, H. Amini, K.S. Fathi, K. Moharamzadeh, E. Sokullu, R. Rahbarghazi, Application of microneedle patches for drug delivery; Doorstep to novel therapies, J. Tissue Eng. 13 (2022) 1768575694.
[23] F. Qu, R. Geng, Y. Liu, J. Zhu, Advanced nanocarrier- and microneedle-based transdermal drug delivery strategies for skin diseases treatment, Theranostics 12 (2022) 3372–3406.
[24] D. Yang, M. Chen, Y. Sun, Y. Jin, C. Lu, X. Pan, G. Quan, C. Wu, Microneedle-mediated transdermal drug delivery for treating diverse skin diseases, Acta Biomater. 121 (2021) 119–133.
[25] M. Overchuk, R.A. Weersink, B.C. Wilson, G. Zheng, Photodynamic and photothermal therapies: synergy opportunities for nanomedicine, ACS Nano 17 (2023) 7979–8003.
[26] X. He, S. Zhang, Y. Tian, W. Cheng, H. Jing, Research progress of nanomedicine-based mild photothermal therapy in tumor, Int. J. Nanomed. 18 (2023) 1433–1468.
[27] S.G. Alamdari, M. Amini, N. Jalilzadeh, B. Baradaran, R. Mohammadzadeh, A. Mokhtarzadeh, F. Oroojalian, Recent advances in nanoparticle-based photothermal therapy for breast cancer, J. Contr. Release 349 (2022) 269–303.
[28] L. Zhao, X. Zhang, X. Wang, X. Guan, W. Zhang, J. Ma, Recent advances in selective photothermal therapy of tumor, J. Nanobiotechnol. 19 (2021) 335.
[29] J.J. Hu, Y.J. Cheng, X.Z. Zhang, Recent advances in nanomaterials for enhanced photothermal therapy of tumors, Nanoscale 10 (2018) 22657–22672.
[30] Z. Zhang, L. Xie, Y. Ju, Y. Dai, Recent advances in metal-phenolic networks for cancer theranostics, Small 17 (2021) e2100314.
[31] P. Liu, X. Shi, S. Zhong, Y. Peng, Y. Qi, J. Ding, W. Zhou, Metal-phenolic networks for cancer theranostics, Biomater. Sci. 9 (2021) 2825–2849.
[32] H. Wang, D. Wang, J. Yu, Y. Zhang, Y. Zhou, Applications of metal-phenolic networks in nanomedicine: a review, Biomater. Sci. 10 (2022) 5786–5808.
[33] Z. Guo, W. Xie, J. Lu, X. Guo, J. Xu, W. Xu, Y. Chi, N. Takuya, H. Wu, L. Zhao, Tannic acid-based metal phenolic networks for bio-applications: a review, J. Mater. Chem. B 9 (2021) 4098–4110.
[34] N. Xu, A. Hu, X. Pu, J. Li, X. Wang, J. Wang, Z. Huang, X. Liao, G. Yin, Fe(iii)-chelated polydopamine nanoparticles for synergistic tumor therapies of enhanced photothermal ablation and antitumor immune activation, ACS Appl. Mater. Interfaces 14 (2022) 15894–15910.
[35] X. Zhu, B. Guan, Z. Sun, X. Tian, X. Li, Fabrication of an injectable hydrogel with inherent photothermal effects from tannic acid for synergistic photothermal-chemotherapy, J. Mater. Chem. B 9 (2021) 6084–6091.
[36] X. Jiang, B.R. Stockwell, M. Conrad, Ferroptosis: mechanisms, biology and role in disease, Nat. Rev. Mol. Cell Biol. 22 (2021) 266–282.
[37] Y. Mou, J. Wang, J. Wu, D. He, C. Zhang, C. Duan, B. Li, Ferroptosis, a new form of cell death: opportunities and challenges in cancer, J. Hematol. Oncol. 12 (2019) 34.

[38] Q. Liu, Y. Zhao, H. Zhou, C. Chen, Ferroptosis: challenges and opportunities for nanomaterials in cancer therapy, Regen. Biomater. 10 (2023) rbad4.
[39] J. Liu, W. Zhong, R. Wang, P. Wang, G. Tong, M. Chai, Y. Sun, T. Zhu, C. Huang, S. Yang, X. Zhou, D. Mou, Y. Cai, Macrophage ferroptotic resistance is required for the progression of infantile hemangioma, J. Am. Heart Assoc. 14 (2025) e34261.
[40] X. Chen, R. Kang, G. Kroemer, D. Tang, Broadening horizons: the role of ferroptosis in cancer, Nat. Rev. Clin. Oncol. 18 (2021) 280–296.
[41] C. Zhang, X. Liu, S. Jin, Y. Chen, R. Guo, Ferroptosis in cancer therapy: a novel approach to reversing drug resistance, Mol. Cancer 21 (2022) 47.
[42] H. Wang, Y. Cheng, C. Mao, S. Liu, D. Xiao, J. Huang, Y. Tao, Emerging mechanisms and targeted therapy of ferroptosis in cancer, Mol. Ther. 29 (2021) 2185–2208.
[43] Z. Li, X. Wu, W. Wang, C. Gai, W. Zhang, W. Li, D. Ding, Fe(ii) and tannic acid-cloaked mof as carrier of artemisinin for supply of ferrous ions to enhance treatment of triple-negative breast cancer, Nanoscale Res. Lett. 16 (2021) 37.
[44] Q. Wang, Y. Sun, S. Li, P. Zhang, Q. Yao, Synthesis and modification of zif-8 and its application in drug delivery and tumor therapy, RSC Adv. 10 (2020) 37600–37620.
[45] E. Boedtkjer, S.F. Pedersen, The acidic tumor microenvironment as a driver of cancer, Annu. Rev. Physiol. 82 (2020) 103–126.
[46] Y. Liu, P. Bhattarai, Z. Dai, X. Chen, Photothermal therapy and photoacoustic imaging via nanotheranostics in fighting cancer, Chem. Soc. Rev. 48 (2019) 2053–2108.
[47] D. Tang, X. Chen, R. Kang, G. Kroemer, Ferroptosis: molecular mechanisms and health implications, Cell Res. 31 (2021) 107–125.
[48] F. Ursini, M. Maiorino, Lipid peroxidation and ferroptosis: the role of gsh and gpx4, Free Radic. Biol. Med. 152 (2020) 175–185.
[49] J. Zhu, X. Tang, Y. Jia, C.T. Ho, Q. Huang, Applications and delivery mechanisms of hyaluronic acid used for topical/transdermal delivery - a review, Int. J. Pharm. 578 (2020) 119127.
[50] X. Li, M. Jiang, S. Zeng, H. Liu, Polydopamine coated multifunctional lanthanide theranostic agent for vascular malformation and tumor vessel imaging beyond 1500 nm and imaging-guided photothermal therapy, Theranostics 9 (2019) 3866–3878.